Journal of Advanced Research 24 (2020) 191–203

Contents lists available at ScienceDirect

Journal of Advanced Research

journal homepage: www.elsevier.com/locate/jare

Electrostatic self-assembly of pFe$_3$O$_4$ nanoparticles on graphene oxide: A co-dispersed nanosystem reinforces PLLA scaffolds

Wenjing Yang [a,b,1], Yancheng Zhong [c,d,1], Chongxian He [a], Shuping Peng [c,d], Youwen Yang [a], Fangwei Qi [a], Pei Feng [b], Cijun Shuai [a,b,e,*]

[a] Institute of Bioadditive Manufacturing, Jiangxi University of Science and Technology, Nanchang 330013, China
[b] State Key Laboratory of High Performance Complex Manufacturing, College of Mechanical and Electrical Engineering, Central South University, Changsha 410083, China
[c] School of Basic Medical Science, Central South University, Changsha 410083, China
[d] School of Energy and Machinery Engineering, Jiangxi University of Science and Technology, Nanchang 330013, China
[e] Shenzhen Institute of Information Technology, Shenzhen 518172, China

GRAPHICAL ABSTRACT

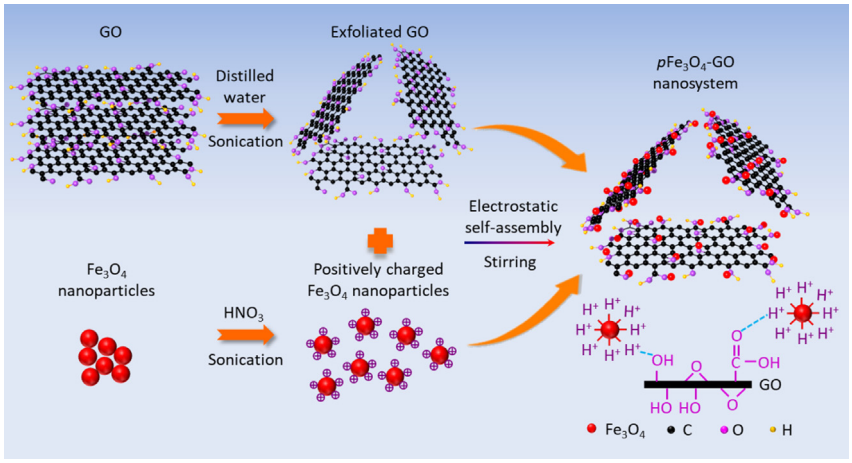

ARTICLE INFO

Article history:
Received 28 January 2020
Revised 12 April 2020
Accepted 15 April 2020
Available online 22 April 2020

Keywords:
Fe_3O_4
Graphene oxide
Co-dispersed pFe$_3$O$_4$-GO nanosystem

ABSTRACT

Cell responses and mechanical properties are vital for scaffold in bone regeneration. Fe_3O_4 nanoparticles with excellent magnetism can provide magnetic stimulation for cell growth, while graphene oxide (GO) nanosheets are commonly used as reinforcement phases due to their high strength. However, Fe_3O_4 or GO is tended to agglomerate in matrix. In present study, a novel co-dispersed Fe_3O_4-GO nanosystem was constructed through electrostatic self-assembly of positively charged Fe_3O_4 (pFe$_3$O$_4$) on negatively charged GO nanosheets. In the nanosystem, pFe$_3$O$_4$ nanoparticles and GO nanosheets support each other, which effectively alleviates the π-π stacking between GO nanosheets and magnetic attraction between pFe$_3$O$_4$ nanoparticles. Subsequently, the nanosystem was incorporated into poly $_L$-lactic acid (PLLA) scaffolds fabricated using selective laser sintering. The results confirmed that the pFe$_3$O$_4$-GO nanosystem

Peer review under responsibility of Cairo University.

* Corresponding author at: State Key Laboratory of High Performance Complex Manufacturing, College of Mechanical and Electrical Engineering, Central South University, Changsha 410083, China.
E-mail address: shuai@csu.edu.cn (C. Shuai).

[1] These authors contributed equally to this work.

https://doi.org/10.1016/j.jare.2020.04.009
2090-1232/

Cell responses
Mechanical properties

exhibited a synergistic enhancement effect on stimulating cell responses by integrating the capturing effect of GO and the magnetic simulation effect of pFe$_3$O$_4$. The activity, proliferation and differentiation of cells grown on scaffolds were significantly enhanced. Moreover, the nanosystem also exhibited a synergistic enhancement effect on mechanical properties of scaffolds, since the pFe$_3$O$_4$ loaded on GO improved the efficiency of stress transfer in matrix. The tensile stress and compressive strength of scaffolds were increased by 67.1% and 132%, respectively. In addition, the nanosystem improved the degradation capability and hydrophilicity of scaffolds.

Introduction

Bone scaffolds not only need to provide temporary mechanical support, but also can stimulate cell responses. Biopolymer, such as poly L-lactic acid (PLLA), polycaprolactone (PCL) and polyglycolic acid are extensively studied as bone scaffold materials due to their good biocompatibility, biodegradability and processability [1–3]. While weak cell responses and insufficient mechanical strength limit their further application in bone regeneration.

Recently, Fe$_3$O$_4$ nanoparticles have attracted tremendous interests owing to their excellent superparamagnetism, large specific surface area and good biocompatibility [4,5]. Cai et al. confirmed that the incorporation of Fe$_3$O$_4$ into PLLA scaffolds stimulated the proliferation of MC3T3-E1 cells [6]. Yun et al. found that the addition of the Fe$_3$O$_4$ nanoparticles in PCL scaffold enhanced osteogenic differentiation [7]. Meanwhile, GO has been widely incorporated into scaffolds for mechanical enhancement [8,9]. Song et al. incorporated GO into PCL nanofiber scaffolds, and found that tensile strength significantly increased [10]. Hence, combination of Fe$_3$O$_4$ and GO may be a promising countermeasure to simultaneously improve cell responses and mechanical properties. However, Fe$_3$O$_4$ nanoparticles or GO nanosheets tend to aggregate in polymer matrix due to the magnetic attraction of Fe$_3$O$_4$ or π-π stacking of GO as well as their strong polarity, which hinders the full play of their reinforcing effect [11,12].

As commonly known, GO nanosheets are highly negatively charged. Hence, a co-dispersed Fe$_3$O$_4$-GO nanosystem may be constructed by electrostatic self-assembly after introducing positive charged Fe$_3$O$_4$ nanoparticles. In detail, the positive charged Fe$_3$O$_4$ nanoparticles may obtained by adsorbing hydrogen ions (H^+) in nitric acid, whereas the negatively charged GO nanosheets are result from the ionization of carboxylic acid and phenolic hydroxyl groups in aqueous solution [13]. In the co-dispersed Fe$_3$O$_4$-GO nanosystem, Fe$_3$O$_4$ nanoparticles and GO nanosheets support each other, which may effectively alleviate the π-π stacking between GO nanosheets and magnetic attraction between Fe$_3$O$_4$ nanoparticles, thereby promoting their respective dispersion. On the one hand, GO possesses abundant oxygen-containing functional groups, numerous negative charges, etc., which enable it to interact with cell membrane and capture cells [14]. In this condition, Fe$_3$O$_4$ nanoparticles loaded on GO nanosheets may contact with cells closer, thereby providing local enhanced magnetic stimulation for cells. On the other hand, Fe$_3$O$_4$ nanoparticles loaded on high-strength GO nanosheets (~130 GPa) may increase efficiency of stress transfer and thus decrease the deformation of polymer matrix under external force, synergistic reinforcing the mechanical properties.

In the present study, a co-dispersed pFe$_3$O$_4$-GO nanosystem was synthesized by electrostatic self-assembly of pFe$_3$O$_4$ nanoparticles on GO nanosheets. Then, the nanosystem was incorporated into PLLA scaffolds fabricated by selective laser sintering (SLS) to stimulate cell responses and improve mechanical properties. The mechanical strengthening mechanism of the nanosystem was discussed. Furthermore, the magnetic property of the scaffolds and their effect on cell adhesion, viability, proliferation and differentiation were systematically studied. Additionally, a cell response mechanism of the nanosystem was discussed.

Materials and method

Materials

Medical-grade PLLA powder with number-average molecular weight of 150 kDa were provided by Shenzhen Polymtek Biomaterial Co., Ltd. (Shenzhen, China). Fe$_3$O$_4$ nanoparticles with average particle size of 10 nm were purchased from Aladdin Chemistry Co. Ltd. (Shanghai, China). GO nanosheets with lateral size of 1–5 μm and thickness of 0.8 nm were obtained from Chengdu Organic Chemistry Co. Ltd. of Chinese Academy of Sciences (Chengdu, China).

Synthesis of pFe$_3$O$_4$-GO nanosystem

The synthetic procedure of pFe$_3$O$_4$-GO nanosystem was shown in Fig. 1. Briefly, 0.15 g of GO was placed in 150 mL of distilled water, followed by ultrasonicating for 1 h to activate the surface groups located on GO. Meanwhile, 0.75 g of Fe$_3$O$_4$ nanoparticles was dispersed in 1 mol/L HNO_3 and then ultrasonicated for 30 min, aiming to achieve positively charged Fe$_3$O$_4$ nanoparticles (pFe$_3$O$_4$) by adsorbing H^+ in HNO_3. Then, pFe$_3$O$_4$ were transferred to GO suspension. Subsequently, the mixture was aged at vigorous stirring for 3 h to assure that the anion exchange sites of the GO were fully saturated with pFe$_3$O$_4$. Afterward, the pFe$_3$O$_4$-GO nanosystem was collected by utilizing an external magnetic field and centrifuging to remove redundant GO nanosheets and unbounded pFe$_3$O$_4$ nanoparticles, followed by washing using deionized water repeatedly. Finally, the obtained pFe$_3$O$_4$-GO nanosystem was vacuum-dried at 60 °C. According to the effective control of the feeding mass ratio of pFe$_3$O$_4$ to GO, three types of pFe$_3$O$_4$-GO nanosystem (mpFe$_3$O$_4$:mGO = 5, 10, 15) were synthesized, which were defined as 5Fe-GO, 10Fe-GO and 15Fe-GO nanosystem, respectively.

Preparation of nanocomposite scaffolds

In the present study, PLLA was served as matrix material because of its good biocompatibility, biodegradability and processability. Prior to the preparation of nanocomposite scaffolds, PLLA/pFe$_3$O$_4$-GO nanocomposite powders were synthesized. Briefly, 0.75 g pFe$_3$O$_4$-GO nanosystem was putted into beaker containing 50 mL of ethanol. After 30 min of ultrasound, the pFe$_3$O$_4$-GO-ethanol suspension was dripped into PLLA-ethanol solution (0.05 g/mL), in which the feeding mass ratios of pFe$_3$O$_4$-GO to PLLA were effectively controlled at 0 wt%, 3 wt%, 6 wt%, 9 wt% or 12 wt%. Subsequently, the above mixture solution was ultrasonicated for another 1 h, followed by mechanical stirring for 90 min. Afterwards, the mixtures were centrifuged, vacuum-dried and mechanical milling to achieve nanocomposite powders.

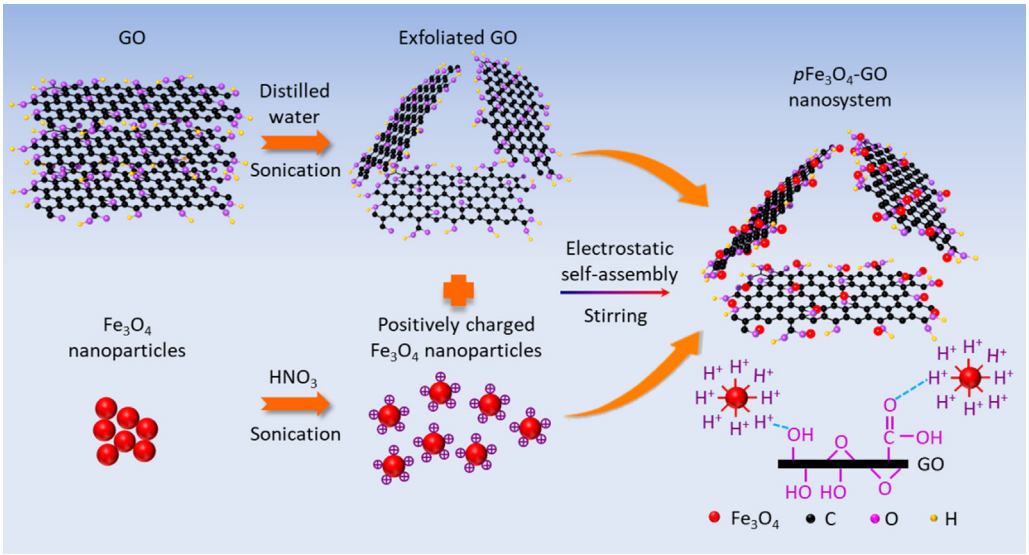

Fig. 1. A schematic illustration of the synthetic route of pFe$_3$O$_4$-GO nanosystem.

The nanocomposite scaffolds were prepared by SLS process. Typically, laser beam accurately scanned the powder bed based on the given model. The laser energy density resulted in the scanned nanocomposite powders rapidly reached the melting point of PLLA powders, which caused the rapid melting and solidification of the PLLA. Meanwhile, the 10Fe-GO nanosystem still retained their intrinsic morphologies and structures because of their high thermal stabilities relative to the PLLA matrix. After sintering each layer, the powder bed fell one layer of powder thickness (0.15 mm), followed by spreading a new layer of powder. Repeating the laser sintering process until the given program was completed. During the whole sintering process, the process parameters were maintained at 3.2 W laser power, 120 mm/s scanning speed and 1 mm scanning spacing. In order to facilitatly distinguish the nanocomposite scaffolds, the scaffolds were defined as 0NC, 3NC, 6NC, 9NC and 12NC scaffolds based on the content of nanosystem in the PLLA matrix, respectively.

Characterization

Transmission electron microscopy (TEM) images of Fe$_3$O$_4$, GO, 5Fe-GO, 10Fe-GO and 15Fe-GO nanosystem were obtained using a Jeol 2100F TEM operated at 200 kV. High-resolution TEM (HRTEM) and selection electron diffraction (SAED) were also performed. Zeta potential of GO, Fe$_3$O$_4$, pFe$_3$O$_4$ and 10Fe-GO were measured at a concentration of 1 mg/mL by Malvern Zetasizer-nano. The chemical characterization of 10Fe-GO nanosystem and 9NC powders were performed on a Thermo ESCALAB 250Xi X-ray photoelectron spectrometer (XPS). The chemical groups of the nanosystem were observed by a FTIR-650 Fourier transform infrared spectrometer (FTIR) in spectral range of 500–4000 cm^{-1}. Morphological observations of scaffolds were carried out under a Phenom proX scanning electron microscope (SEM) after sputter-coated with gold (6 mA, 60 s).

Magnetization curves of the scaffolds were obtained using a SQUID vibrating sample magnetometer (VSM) under a magnetic field of ±20,000 Oe. Thermal decomposition of scaffolds was detected by a STA-200 thermo-gravimetric analyzer (TGA) with a temperature range of 30–600 °C. In order to reduce the influence of heating rate, atmosphere and sample dosage on thermal analysis, they were set at a constant 20 °C/min, nitrogen and 15 mg. The mechanical properties including compressive and tensile strength of the scaffolds were determined by compression and tensile tests on a CMTS5205 universal testing machine. The tests were performed in quintuplicate. Throughout the whole testing, loading rate was maintained at 0.5 mm/min. The scaffold specimens ($5 \times 4 \times 3$ mm^3) were used for the compression test, while dumbbell specimens (L0 = 10.1 mm, h = 2.2 mm) were used for the tensile tests. The sample size was determined according to ISO 604 and ISO 527-2 (small specimen). The morphologies of tensile section were observed by SEM.

In order to evaluate the degradation capability of the scaffolds, the pH values and degradation rate were determined after immersing 7 days, 14 days, 21 days and 28 days in phosphate buffered solution (PBS) solution at 37 °C. In detail, the original mass (M_0) of specimens was determined using an FA124 electronic analytical balance, followed by immersing in PBS solution (10 mL). Subsequently, the specimen-solutions were placed into a constant temperature incubator (37 °C). At the predetermined time point, the pH values of each specimen-solution were measured via a FE28 pH meter, and then the specimens were taken out, cleaned and dried. Afterward, the residual mass (M_1) of each specimen was determined, and the weight loss rate was then calculated according to the following formula:

$$\text{Weight loss } (\%) = \frac{M_0 - M_1}{M_0} \times 100\% \quad (1)$$

In addition, the degradation morphology of the scaffold specimens after immersing 28 days was observed by SEM.

Cell culture

Disk scaffold specimens ($\phi 8 \times 2$ mm^3) were selected to investigate the cytocompatibility of the scaffolds, in which MG-63 cells (Institute of Reproductive and Stem Cell Engineering, Xiangya Medical College, Central South University, China) were selected in the investigation. The cells at a density of 10^4 cells/scaffold were seeded in DMEM which including 10% fetal bovine serum and 1% penicillin/streptomycin sulfate supplement. Throughout the culture process, the cell-scaffold constructs were placed in a constant atmosphere with 5% CO_2 at 37 °C.

Cell adhesion morphology on scaffolds was observed using SEM. At the predetermined time point (1, 3 and 5 days), the cell-scaffold constructs were extracted from the culture medium and gently

washed with PBS to eliminate unattached cells. Subsequently, the cell-scaffold constructs were fixed using 2.5% glutaraldehyde, washed using PBS, dehydrated using ethanol and dried at 37 °C. Afterwards, cell-scaffold constructs were sputtered by gold prior to facilitate morphological observation.

Cell viability on scaffolds was assessed by live/dead viability/cytotoxicity test. After 1, 3 and 5 days of culturing, cell-scaffold constructs were collected and washed. Then, they were cultivated in PBS supplemented with 2 μM calcein-AM and 1 μM ethidium homodimer (EthD-1) for 30 min, in which the live cells were strained green while dead cells were strained red. Subsequently, the stained cells were visualized using a BX51 fluorescence microscope.

Cell proliferation on scaffolds was quantitatively analyzed by Cell Counting Kit-8 (CCK-8) assay. Briefly, the cell-scaffold constructs were collected at the predetermined culture periods (1, 3 and 5 days). After washing using PBS, they were transferred into fresh culture medium supplemented with CCK-8 reagent, and then incubated for 30 min at 37 °C. Afterwards, the absorbance of the above solution was quantified measured at 450 nm using a Biotek microplate reader. Three parallel experiments were carried out for each group.

Osteogenic differentiation of cells on scaffolds was determined using alkaline phosphatase (ALP) activity according to the manufacturer's instruction. After 1, 4 and 7 days of incubation, the cell-scaffold constructs were gently washed with PBS. Then, 0.25% trypsin solution was utilized to remove the adherent cells. Subsequently, the cells were rinsed with PBS and stained using LabAssayTM ALP kit. The stained cells were visualized by a Nikon TE2000U inverted microscope.

Statistical analysis

All quantitative experimental data was presented as means ± standard deviations. Statistical differences between groups were analyzed using either unpaired two-tailed Student's *t*-test or One Way ANOVA when necessary. Significant differences were regarded when P value lower than 0.05 ($^{*}P < 0.05$), 0.01 ($^{**}P < 0.01$) and 0.005 ($^{***}P < 0.005$).

Results and discussion

pFe_3O_4-GO nanosystem

Zeta potentials of GO, Fe_3O_4, pFe_3O_4 and 10Fe-GO were detected and shown in Fig. 2a. It can be seen that the GO nanosheets were highly negatively charged (−34.6 mV), which was attributed to the ionization of carboxylic acid and phenolic hydroxyl groups located on GO nanosheets in aqueous solution. The average zeta potential of Fe_3O_4 was −13.2 mV, while the zeta potential of pFe_3O_4 was 23.9 mV, indicating that the pFe_3O_4 were highly positively charged. It was apparently a result of the absorption of hydrogen ions (H^+) in HNO_3. Remarkably, the zeta potential of 10Fe-GO was −16.7 mV which was higher than that of GO nanosheets and lower than that of pFe_3O_4, demonstrating that pFe_3O_4 have been successfully self-assembled on the surface of GO nanosheets.

FTIR spectra of pFe_3O_4 nanoparticles, GO nanosheets and pFe_3O_4-GO nanosystem were presented in Fig. 2b. As for pFe_3O_4, the absorption bands at 563 cm^{-1} was ascribed to Fe—O stretching vibration. As for GO, the absorption bands at 1725 cm^{-1} and 1627 cm^{-1} were assigned to the stretching vibrations of C═O and C—O, while the bands at 1392 cm^{-1} and 1052 cm^{-1} can be attributed to O—H deformations and stretching vibrations of C—O [15]. As expected, the spectrum of pFe_3O_4-GO nanosystem was almost similar with that of GO, indicating the structure of GO was kept well. Note that the characteristic absorption band at 563 cm^{-1} proved that pFe_3O_4 nanoparticles were successfully self-assembled on GO nanosheets.

The wide scan XPS spectrum of the pFe_3O_4-GO nanosystem exhibited the sharp peaks approximately 710, 530 and 280 eV (Fig. 2c), which assigned to the characteristic peaks of Fe 2p, O1s and C1s, respectively. In the Fe 2p spectrum (Fig. 2d), the peaks at 711.4 and 724.6 eV attributed to the Fe $2p_{1/2}$ and Fe $2p_{3/2}$ spin–orbit peaks of Fe_3O_4 [16], confirming that the successfully self-assembly of pFe_3O_4 nanoparticles on GO nanosheets. The O1s spectrum has been fitted by four peaks corresponding to oxygen (Fig. 2e). The main peak at 530.3 eV was assigned to Fe—O bond. The peak at 531.8 eV was due to C(O)OH while the peaks at 532.2 eV and 533.8 eV could be attributed to C═O and C—OH bonds [17]. The corresponding C1s XPS spectrum for pFe_3O_4-GO nanosystem revealed a peak with four main components (Fig. 2f), one at 284.4 eV related to —C═C, and the peak at 285.9 eV was assigned to C—O bond [18]. The component at 287.6 eV and 289.1 eV were usually corresponding to C═O and O—C═O bonds. The O1s and C1s spectra indicated that the structure and chemical composition of GO were kept well after loading pFe_3O_4.

The morphology of GO nanosheets, 5Fe-GO, 10Fe-GO and 15Fe-GO nanosystem were characterized by TEM, as shown in Fig. 3. Clearly, the GO sheet possessed large surface area with irregular shape (Fig. 3a). The morphologies of 5Fe-GO, 10Fe-GO and 15Fe-GO nanosystem which had different mass ratios of Fe_3O_4 nanoparticles to GO were presented in Fig. 3b–d. It could be seen that the pFe_3O_4 nanoparticles were anchored onto the surface of the GO nanosheets, owing to the electrostatic self-assembly between the positively charged Fe_3O_4 and the negatively charged GO. The average particle size of pFe_3O_4 nanoparticles on GO was approximately 10.5 nm (inset in Fig. 3b). Compared with the 5Fe-GO and 15Fe-GO nanosystem (Fig. 2b and d), the pFe_3O_4 nanoparticles homogeneously assembled on GO nanosheets in 10Fe-GO nanosystem (Fig. 3c), indicating the appropriate feeding mass ratio of pFe_3O_4 to GO. In the 10Fe-GO nanosystem, the uniform electrostatic self-assembly enabled pFe_3O_4 and GO to support each other, effectively increasing the interlamellar space of GO and interparticle space of pFe_3O_4, thus promoting their respective dispersion. In the enlarged image (Fig. 3e), the lattice fringe spacing of 0.76 nm and 0.25 nm were belong to GO sheet and pFe_3O_4 nanoparticles [19,20], respectively. The selected-area electron diffraction pattern (Fig. 3f) obtained from Fig. 3c (red circle) exhibited the diffraction rings of the (3 1 1), (4 0 0), (4 2 2) (5 1 1) and (4 4 0), revealing the inverse cubic spinel structure of Fe_3O_4 nanoparticles. The above results confirmed that pFe_3O_4 was successful self-assembled on GO nanosheets. Above all, the 10Fe-GO nanosystem exhibited the best feeding mass ratio of pFe_3O_4 to GO, therefore, it was selected for further study.

According to the above analyses, pFe_3O_4 and GO successfully constructed a co-dispersed nanosystem via electrostatic self-assembly, which was expected to greatly enhance the polymer scaffold. As for the synthesis of various hybrid nanostructures, different interaction ways were employed [21–24]. For instance, Kalarikkal et al. developed nitrogen sulfur doped graphene/Ag nanostructures by hydrothermal assisted strategy [25]. Sayali et al. prepared rGO/TiO_2 nanocomposites using in-situ deposition [26]. Maya et al. synthesized nano tin ferrous oxide decorated graphene oxide by solution combustion technique [27].

Nanocomposites

Morphology of the PLLA and nanocomposites were characterized by SEM. As shown in Fig. 4b, PLLA exhibited an irregular block structure, and nanocomposites possessed similar shape, indicating the incorporation of pFe_3O_4-GO nanosystem didn't significantly

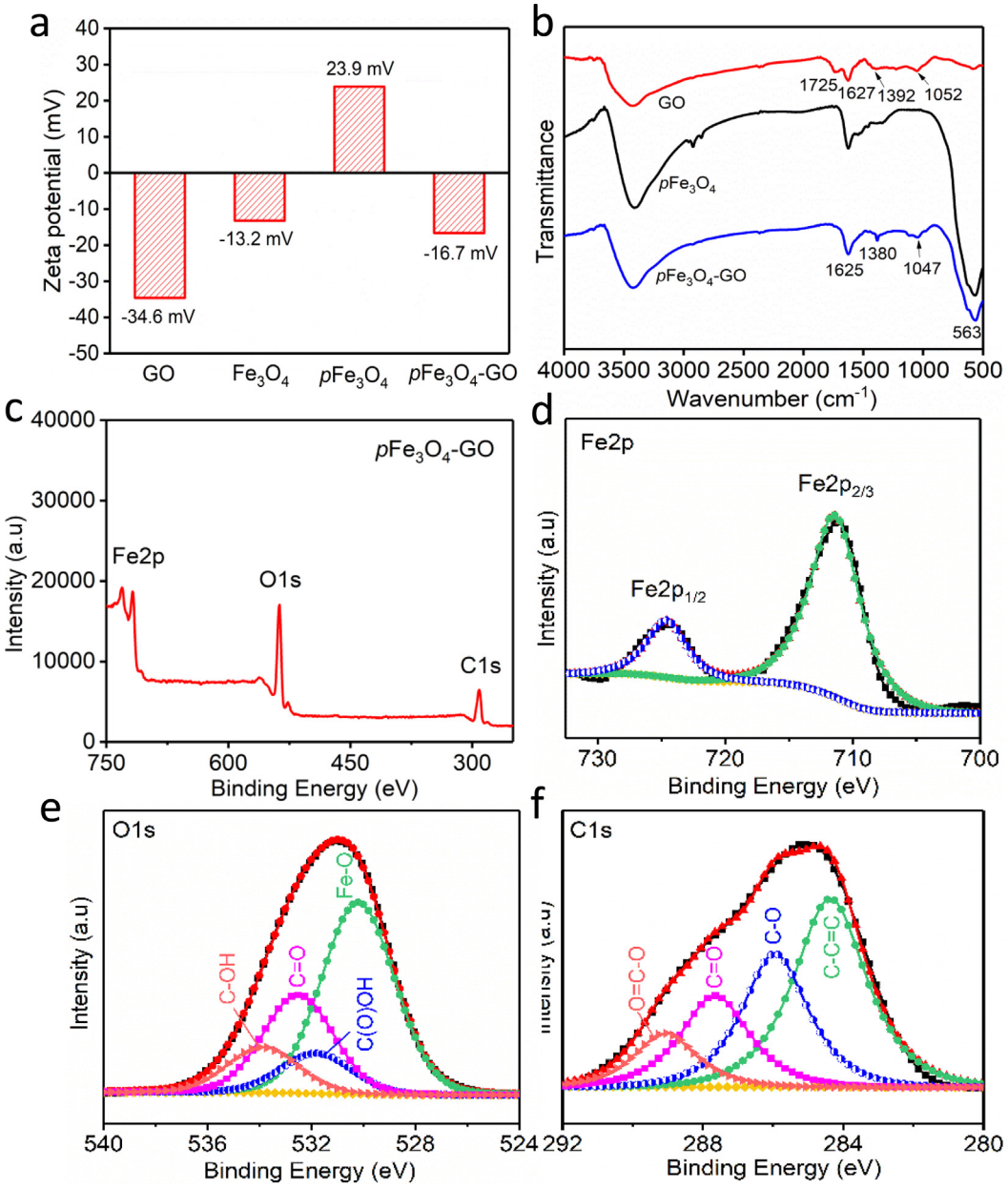

Fig. 2. (a) Zeta potential of GO, Fe_3O_4, pFe_3O_4 and pFe_3O_4-GO. (b) FTIR spectra of GO and pFe_3O_4-GO. (c) XPS characterization of pFe_3O_4-GO nanosystem. XPS survey spectra along with the spectra of (d) Fe2p, (e) O1s and (f) C1s.

change the morphology of PLLA. The chemical composition of PLLA/pFe_3O_4-GO nanocomposites was detected using XPS (Fig. 4c). It could be seen that the characteristic peaks of Fe 2p, O1s and C1s were similar with that of pFe_3O_4-GO nanosystem (Fig. 2c). Similarly, the Fe $2p_{1/2}$ and Fe $2p_{3/2}$ spin–orbit peaks position of nanocomposites were consistent with pFe_3O_4-GO nanosystem. However, the ratio of O1s to C1s peaks in spectrum of nanocomposites differed from that of pFe_3O_4-GO nanosystem, which was due to the introduction of C and O from PLLA.

Scaffold structure, magnetic and thermal behavior

It is well known that scaffolds used for bone regeneration should meet structure and pore size requirements. Pores must be interconnected to favor cell adhesion, growth, proliferation and differentiation within biological scaffolds [28]. For the optimal pore size, it is controversial in literatures due to the fact that bone regeneration is a very complex process. Some studies suggested that the pore size of the scaffold should be between 20 and 1500 μm [29], while others recommend ranges from 150 μm to 600 μm, 200 μm to 1500 μm, or 400 μm to 1200 μm [30]. In present study, nanocomposite scaffolds possessed a three-dimensional interconnected porous structure, as presented in Fig. 5a. The pore dimensions of scaffold were mostly between 600 and 750 μm calculated from SEM images using ImageJ software. They were smaller than the designed model (800 μm), which was the result of the thermal affected zone of laser sintering process. The pore sizes were believed to facilitate cell adhesion and growth as well as guarantee the nutrient and metabolite transport [31].

The magnetic performance of 0NC, 3NC, 6NC, 9NC and 12NC scaffolds was measured using VSM, as shown in Fig. 5b and c. Clearly, it can be seen that the existence of 10Fe-GO nanosystem enhanced saturation magnetization values of scaffolds as com-

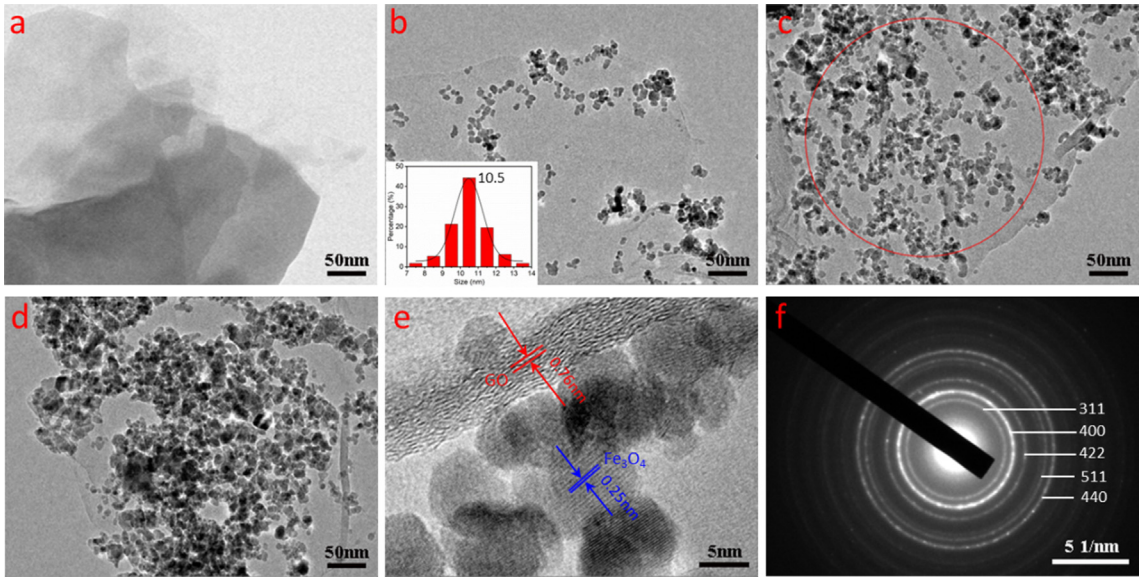

Fig. 3. TEM images of (a) GO, (b) 5Fe-GO, (c) 10Fe-GO and (d) 15Fe-GO nanosystem. Inset in (b) showed the particle size of pFe$_3$O$_4$ nanoparticles on GO with an average size of 10.5 nm. (e) HRTEM images of GO and pFe$_3$O$_4$ nanoparticles in 10Fe-GO nanosystem. (f) selected-area electron diffraction pattern of 10Fe-GO nanosystem (red circle in (c)). (For interpretation of the references to colour in this figure legend, the reader is referred to the web version of this article.)

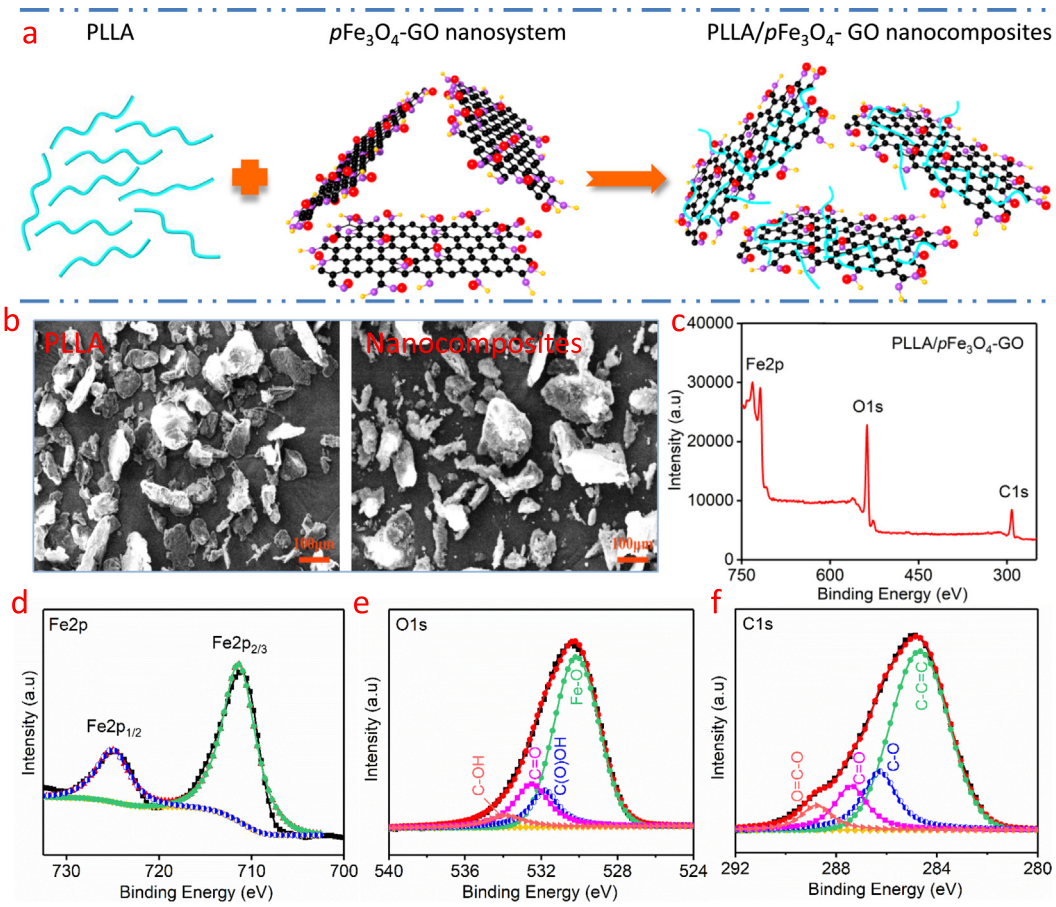

Fig. 4. (a) A schematic illustration of the synthetic route of PLLA/pFe$_3$O$_4$-GO nanocomposites. (b) Morphology of the PLLA powder and nanocomposites. (c–f) XPS spectra of PLLA/pFe$_3$O$_4$-GO nanocomposites.

pared with 0NC (pure PLLA) scaffold (Fig. 5b). The saturation magnetization increased from 0 to 6 emu/g with increasing 10Fe-GO from 0 to 12 wt%, as a result of the magnetization of pFe$_3$O$_4$ nanoparticles in the 10Fe-GO nanosystem by the external magnetic field. In addition, the magnetic performance of scaffolds at low magnetic field range (−50 Oe to 50 Oe) was presented in

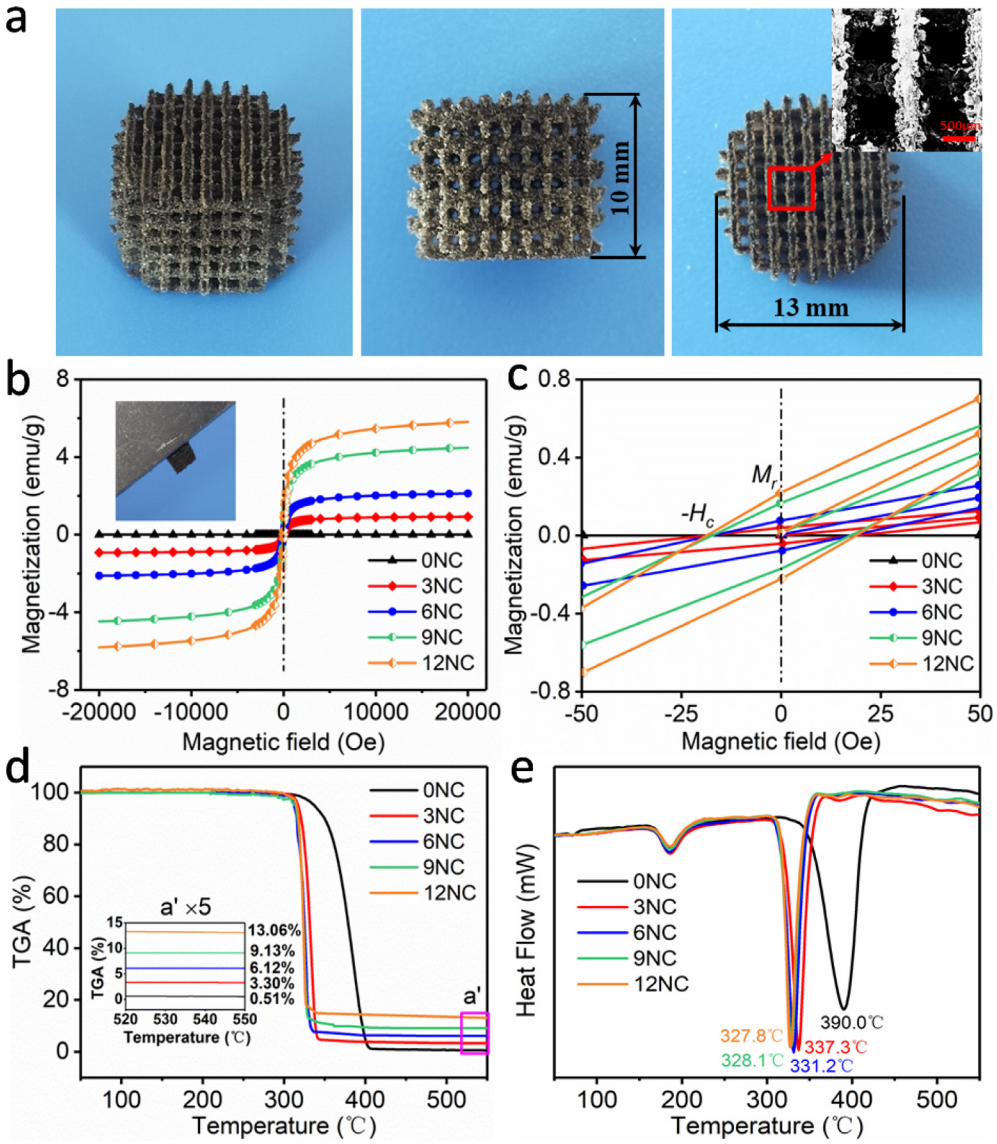

Fig. 5. Structure, magnetic performance and thermal behavior of the scaffolds. (a) Scaffolds with three-dimensional interconnected porous structure. (b) Magnetization curve. (c) Magnetization behavior at low magnetic field (−50 to 50 Oe). (d) TGA and (e) DTG curve.

Fig. 5c. The low coercivity (Hc) and remanence (Mr) indicated that the scaffolds were superparamagnetic, which was conducive to the rapid response of the scaffolds to external magnetic field. Based on our previous study [4,32,33], high saturation magnetization and superparamagnetism of scaffolds was expected to enhance the magnetic stimulation on cells grown on them.

The thermal decomposition process of scaffolds was analyzed using TGA and DTG, as shown in Fig. 5d and e. Obviously, the scaffolds presented weight loss in one step (Fig. 5d). The slight weight loss below 300 °C was attributed to the evaporation of adsorbed water molecules. Thermal decomposition temperature of the 0NC scaffold was between 314 and 407 °C, while the range of decomposition temperature shifted left and narrowed when the 10Fe-GO nanosystem increased from 3 to 12 wt%. Additionally, the residual weight of the 3NC, 6NC, 9NC and 12NC scaffolds was 3.3, 6.12, 9.13 and 13.06 wt%, respectively, which was in good agreement with the content of nanosystem initially added into PLLA matrix. In DTG curves (Fig. 5e), the melting point of the scaffolds didn't change with the addition of 10Fe-GO nanosystem (about 185.2 °C). However, the maximum weightlessness temperatures of 0NC, 3NC, 6NC, 9NC and 12NC scaffolds decreased with increasing 10Fe-GO nanosystem, which were 390 °C, 337.3 °C, 331.2 °C, 328.1 °C and 327.8 °C, respectively. The TGA and DTG analysis results indicated that the incorporation of 10Fe-GO nanosystem catalyzed the decomposition of PLLA matrix.

Mechanical properties

Tensile and compressive tests were performed, aiming to investigate the influence of incorporating 10Fe-GO nanosystem on the mechanical properties of scaffolds. Clearly, the 10Fe-GO nanosystem significantly enhanced the tensile strength, compressive strength and modulus of scaffolds compared with 0NC scaffold (Fig. 6a and b). The tensile stress and strain of the 0NC scaffold was 8.2 MPa and 12.1%, respectively. Encouragingly, the tensile stress and strain improved to 13.7 MPa and 22.1% for 9NC scaffold, which was 67.1% and 82.6% higher than those of 0NC scaffold, respectively. Moreover, the 9NC scaffold also exhibited much higher compressive strength and modulus than those of 0NC scaffold, which were 24.2 MPa and 260 MPa, respectively. It was

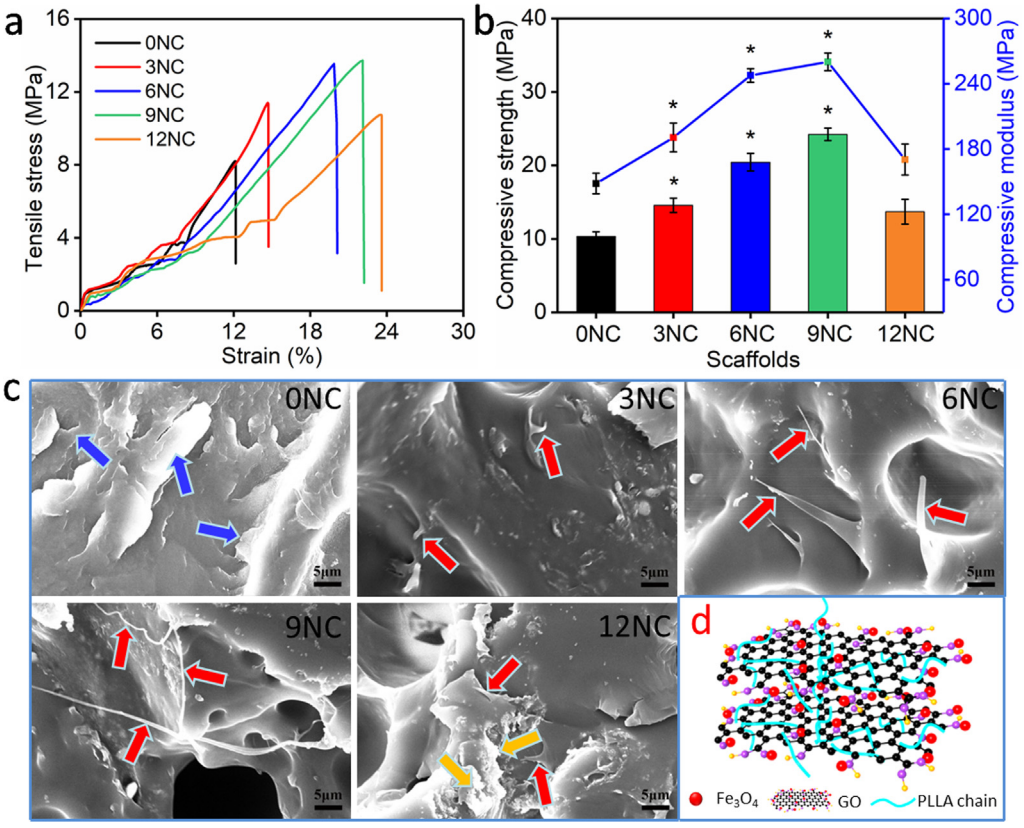

Fig. 6. Mechanical properties of scaffolds. (a) Typical tensile stress–strain curves. (b) Compressive strength and modulus. (c) Morphology of tensile fracture. (d) Interfacial bonding between nanosystem and PLLA chain.

mainly due to the fact that the pFe$_3$O$_4$ nanoparticles and GO nanosheets in 10Fe-GO nanosystem synergistically enhanced the mechanical properties of PLLA matrix. The high modulus could be attributed to interfacial interaction between pFe$_3$O$_4$-GO and PLLA chains. In present study, the hydroxyl and carbonxyl groups on GO nanosheets and oxygen-containing functional groups of PLLA chains were able to form hydrogen bond. In this case, the dispersed pFe$_3$O$_4$-GO nanosyetem could act as a "physical crosslinking points" to form three-dimensional crosslinking network with PLLA chains in the matrix [34,35], thus restricting the mobility of PLLA chains and ultimately improving the modulus. However, after adding 12 wt% 10Fe-GO nanosystem, the mechanical strengths decreased compared with 9NC scaffold. This was due to the defects caused by aggregates in matrix weakened its reinforcing effect, because good dispersion of reinforcer was vital in the mechanical properties of polymer matrix [36,37].

In fact, the reinforcement of mechanical properties of polymer matrix with nano-fillers depends on their interfacial compatibility and good dispersion of nano-fillers [38–42]. As pFe$_3$O$_4$ nanoparticles own magnetic property and large specific surface area, plus their intrinsic interfacial incompatibility with polymers, they tend to aggregate in polymer matrix, thus weakening their reinforcing efficiency. GO possesses abundant functional groups, such as carboxyl, hydroxyl, carbonyl and epoxy, could form hydrogen bond with the PLLA chains, thereby obtaining good interfacial adhesion with PLLA matrix. However, strong π-π stacking between adjacent GO nanosheet leads to their aggregation in PLLA matrix. In the 10Fe-GO nanosystem, pFe$_3$O$_4$ nanoparticles were assembled on GO nanosheets, increasing the distance of the adjacent pFe$_3$O$_4$ nanoparticles and interlamellar space of adjacent GO nanosheets. In this condition, their respective aggregation caused by magnetic mutual attraction or π-π stacking and Van der Waals was effectively hindered, thereby improving their respective dispersion. Moreover, the 10Fe-GO nanosystem possessed good interfacial compatibility with the PLLA matrix due to the good interfacial adhesion between GO and the matrix. As a result, Fe$_3$O$_4$ nanoparticles and GO nanosheets in 10Fe-GO nanosystem synergistically enhanced the stress transfer efficiency in the matrix, thereby reinforcing the PLLA scaffolds. The results were similar to those of Jose et al [34,35,43], in which they also proved the synergism between nano-fillers in strengthening polymer.

In order to better understand the mechanical enhancement effect of 10Fe-GO nanosystem on scaffolds, the tensile fracture mode was observed with SEM (Fig. 6c). The fracture mode of 0NC scaffold was typical brittle fracture, in which cleavage planes with facet presented on the section (blue arrow). Interestingly, the fractures of 3NC, 6NC, 9NC and 12NC scaffolds presented the pull-out of GO nanosheets (red arrow). Especially, GO nanosheets in 9NC scaffold were not only pull-out but also much more curled. These phenomena were attributed to the hydrogen bonding between the hydroxyl and carbonxyl groups on GO nanosheets and oxygen containing functional groups of PLLA chains [12], achieving good interfacial bonding (Fig. 6d). Thus, upon the tensile stressing, the hydrogen bonding firstly occurred to fracture, triggering the slippage of adjacent GO nanosheets [44]. With gradually increased loading, the GO nanosheets would be stretched successively from PLLA matrix due to the continuous breakage of hydrogen bonding, absorbing of more energy. After further loading, the hydrogen bonding was completely destroyed, and the π-π conjugated interaction and friction between adjacent 10Fe-GO nanosystem also dissipated of much more energy, accompanied by the pull-out and curl of GO. Hence, the incorporation of 10Fe-GO nanosystem significantly improved the tensile stress and strain of the scaffolds, revealing the synergistic enhancement effect of pFe$_3$O$_4$ and GO.

However, the excess of nanosystem would act as impurities in 12NC scaffolds (yellow arrow in Fig. 6c), which explained the decreased tensile stress and compressive strength. The phenomenon was well consistent with our previous studies [32,45], serious agglomeration of Fe_3O_4 or GO occurred in PLLA matrix when the addition exceeded 7.5 wt% or 0.9 wt%, respectively. Note that the slight agglomeration of 10Fe-GO nanosystem presented in matrix when its' content was as high as 12 wt%, which was clearly evidenced that the electrostatic self-assembly *p*Fe_3O_4 and GO improved their respective dispersion in matrix, thereby synergistically enhancing mechanical properties.

Degradation properties

In general, good degradation capability of scaffold is required in scaffold-induced bone regeneration [46,47]. Here, the degradation rates of scaffolds in PBS (pH = 7.4) were investigated. As shown in Fig. 7a, the degradation rate of scaffolds increased with time of enzymatic hydrolysis. Actually, enzymatic hydrolysis of polymers is associated with various factors, such as chemical structure, additives, hydrophilic hydrophobic properties of chains, hydrolytic mediums, amount of ester bonds and degree of crystallinity, etc. In the present study, the addition of 10Fe-GO apparently accelerated the degradation of PLLA matrix and especially, the more 10Fe-GO in scaffolds, the higher degradation of the scaffolds was. On the one hand, it was owing to the more 10Fe-GO, the more polar hydrophilic groups (—COOH and —OH) were introduced, thereby improving the hydrophilicity of scaffolds (Fig. 7b). As a result, the 10Fe-GO promoted the penetration of water molecules into PLLA matrix, which caused hydrolytic chain scission of ester groups and thus accelerated hydrolysis of matrix. It was consistent with the typical hydrolysis of high molecular weight polyester [48].

On the other hand, the hydrolytic degradation medium also greatly affected the degradation of scaffolds, especially alkaline solution [49]. Hence, changes in the pH of PBS solution caused by scaffold degradation were tracked. As shown in Fig. 7c, the pH values of all scaffold samples exhibited apparent reduction after immersing for 7 days, which was attributed to the acidic degradation products of PLLA matrix during hydrolysis. It was remarkable that the 3NC, 6NC, 9NC and 12NC scaffolds exhibited higher pH values than the 0NC scaffold after immersing 14 days. Some studies had shown that GO in alkaline solution significantly accelerated the degradation of PLLA than in acidic condition [50]. Based on this point of view, the accelerated degradation of PLLA by GO was related to the weak alkalinity of degradation medium. The degradation morphology of the scaffolds after 28 days immersion also confirmed the accelerated degradation (Fig. 7d). The more the 10Fe-GO nanosystem added, the more holes left on the surface of scaffolds (blue arrow), which caused by hydrolysis of PLLA matrix. This phenomenon agreed with the hydrolytic degradation behavior of PLLA-based composites in alkaline solution [51].

Biocompatibility

Good biocompatibility of scaffold is essential for cell adhesion and growth [52–54]. Based on the above analyses, the 9NC scaffold exhibited the best comprehensive properties that chose to assess the biocompatibility, in which the 0NC scaffold as control. In order to evaluate the interaction between MG63 cells and scaffolds, the cell adhesion and morphology on the scaffolds was observed using SEM after cultivating for 1, 3 and 5 days (Fig. 8a). Obviously, the cells adhered on both 0NC and 9NC scaffolds after 1 day of culture, indicating the biocompatibility of scaffold materials. Encouragingly, cells on 9NC scaffold exhibited a flatter morphology with extended filopodia than that on 0NC scaffold after culturing for

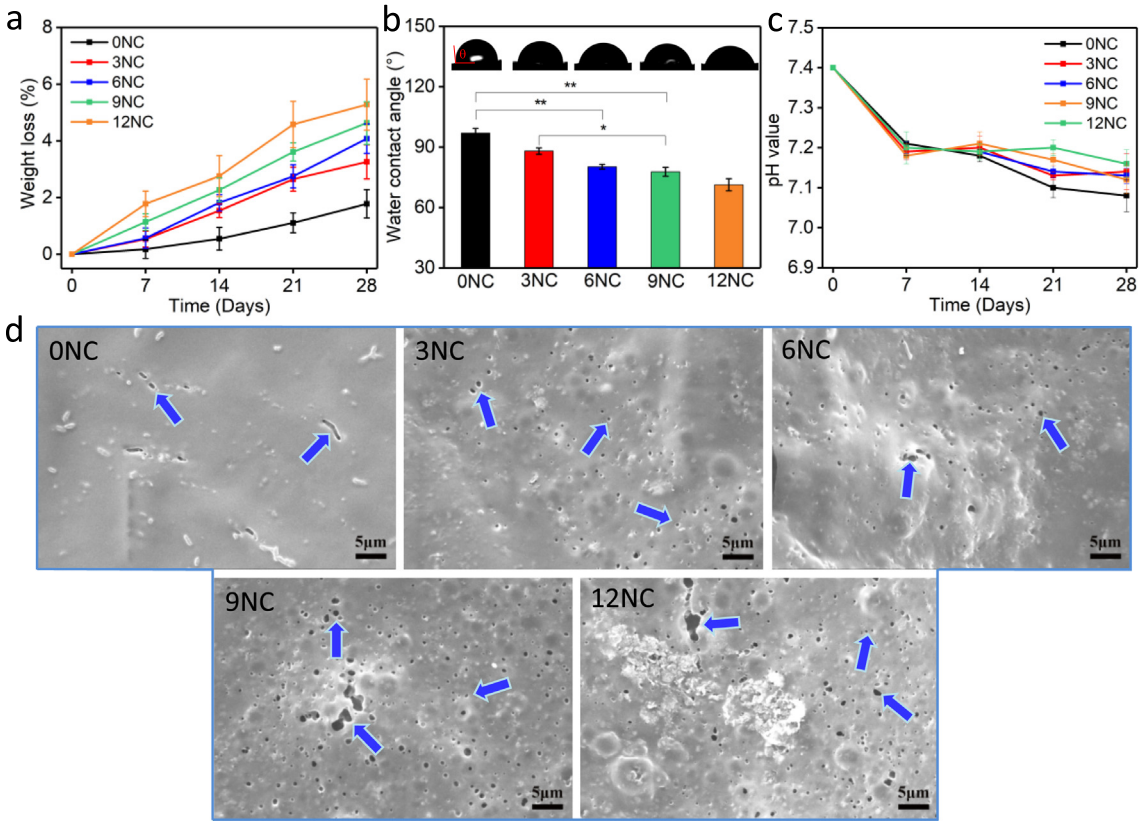

Fig. 7. Degradation behavior of scaffolds. (a) The change of weight loss. (b) Water contact angle. (c) The change of pH values. (d) Depredated morphology of scaffold after immersing for 28 days.

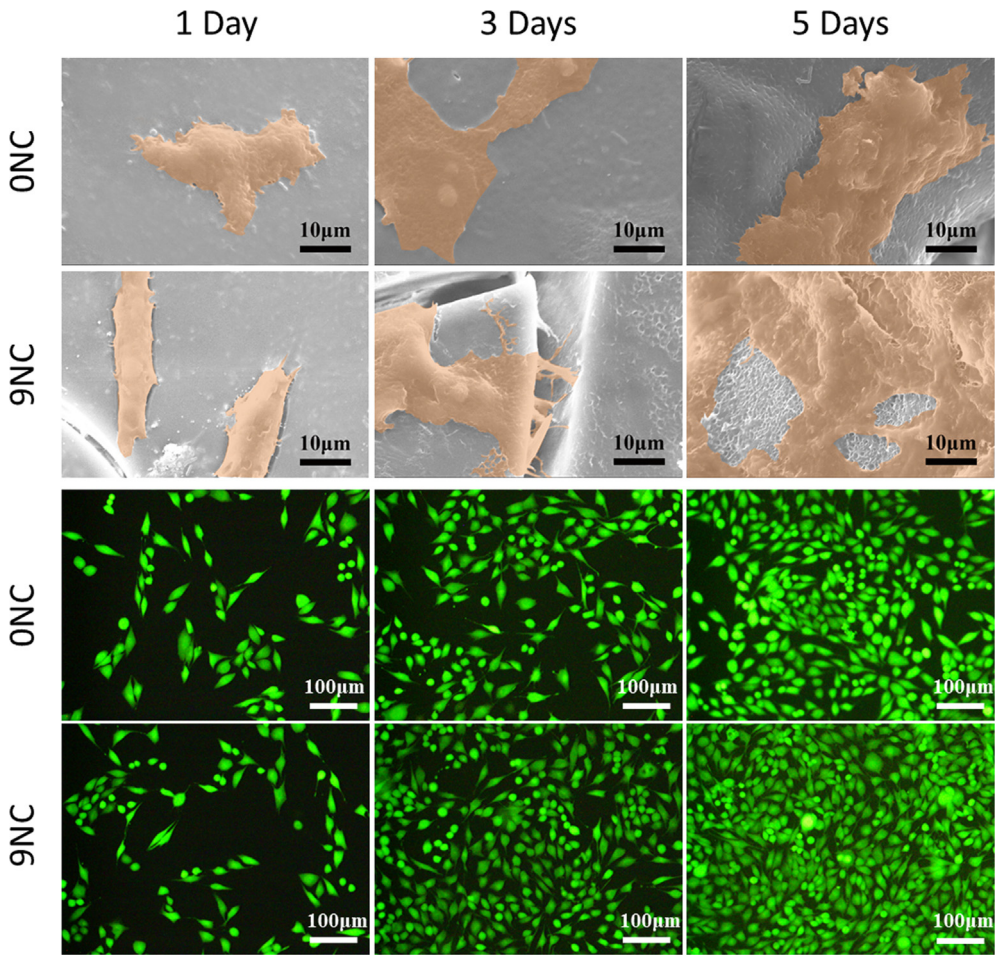

Fig. 8. (a) The adhesion morphology and (b) viability of MG63 cells cultured on 0NC and 9NC scaffolds for 1, 3 and 5 days.

3 days. Moreover, cells remained good adhesion morphology and extended to a wide area on the 9NC scaffold compared with that on 0NC scaffold after 5 days of incubation. It was suggesting that the 9NC scaffold provided more favorable microenvironments for cell adhesion than 0NC scaffold. The enhanced cell adhesion likely attributed to three factors. Firstly, the Fe_3O_4 nanoparticles in matrix served as nanoscale magnetic source contributed to cell adhesion [32,33]. Second, anionic functional groups (COO^- and OH^-) on GO nanosheets adjusted the surface charge and improved the hydrophilicity of scaffold, which provided opportunities for cell adhesion [55]. Thirdly, the uniform dispersion of 10Fe-GO nanosystem in matrix provided more adhesion sites for cell adhesion.

The viability of MG63 cells was evaluated using immunofluorescence and shown in Fig. 8b, where living cells were stained in green. It could be observed that the cells on both 0NC and 9NC scaffolds showed well diffusion morphology, and cell density increased with the extending of culture time, which also confirmed the favorable biocompatibility of scaffold materials. It was worth noting that cell density on 9NC scaffold was higher than that on 0NC scaffold. The high biocompatibility of 9NC scaffold was attributed to the numerous adhesion sites for cells provided by 10Fe-GO nanosystem. Moreover, the COO^- and OH^- groups on GO sheets improved the hydrophilicity and regulated the surface charge of scaffold, thus enhancing cell viability and proliferation. Meanwhile, Fe_3O_4 nanoparticles loaded on GO sheets, which provided a locally enhanced magnetic microenvironment for cells, thus enhancing the cell viability.

The proliferation of MG63 cells on scaffolds was assessed by CCK-8 assay after culturing for 1, 3 and 5 days (Fig. 9a). The absorbance was closely related to the number of live cells. Obviously, the absorbance values gradually increased with the extension of culture time, confirming that the number of live cells increased. Interestingly, the absorbance of 9NC scaffold was higher than that of 0NC scaffold, demonstrating that 10Fe-GO nanosystem had a positive stimulating effect on cell proliferation. To investigate the effects of scaffolds on osteogenic differentiation, ALP activity as one of the markers for early osteoblastic differentiation was detected after culturing cells on 9NC and 0NC scaffolds for 3 and 5 days. As shown in Fig. 9b, the ALP activity level on 9NC scaffolds increased over time, and it was significantly better than that on 0NC scaffolds at the same incubation time. It indicated that the incorporation of 10Fe-GO nanosystem provided a suitable microenvironment for osteogenic differentiation of cells.

The above results confirmed that the presence of 10Fe-GO nanosystem was conducive to cell adhesion and growth, and enhanced cell proliferation and differentiation, which might be attributed to the synergistic stimulation effect of GO nanosheets and $p$$Fe_3O_4$ nanoparticles. A possible synergistic stimulation mechanism of 10Fe-GO nanosystem for osteogenic proliferation and differentiation was shown in Fig. 9c. GO nanosheets possessed numerous oxygen-containing functional groups, which were negative charged, enabled them interact with cell membrane phospholipids and proteins by electrostatic interaction, hydrogen bonding, π-π stacking, etc. [14]. The interaction enabled cells to adsorb on the GO nanosheets and then captured. What's more, the absorbing

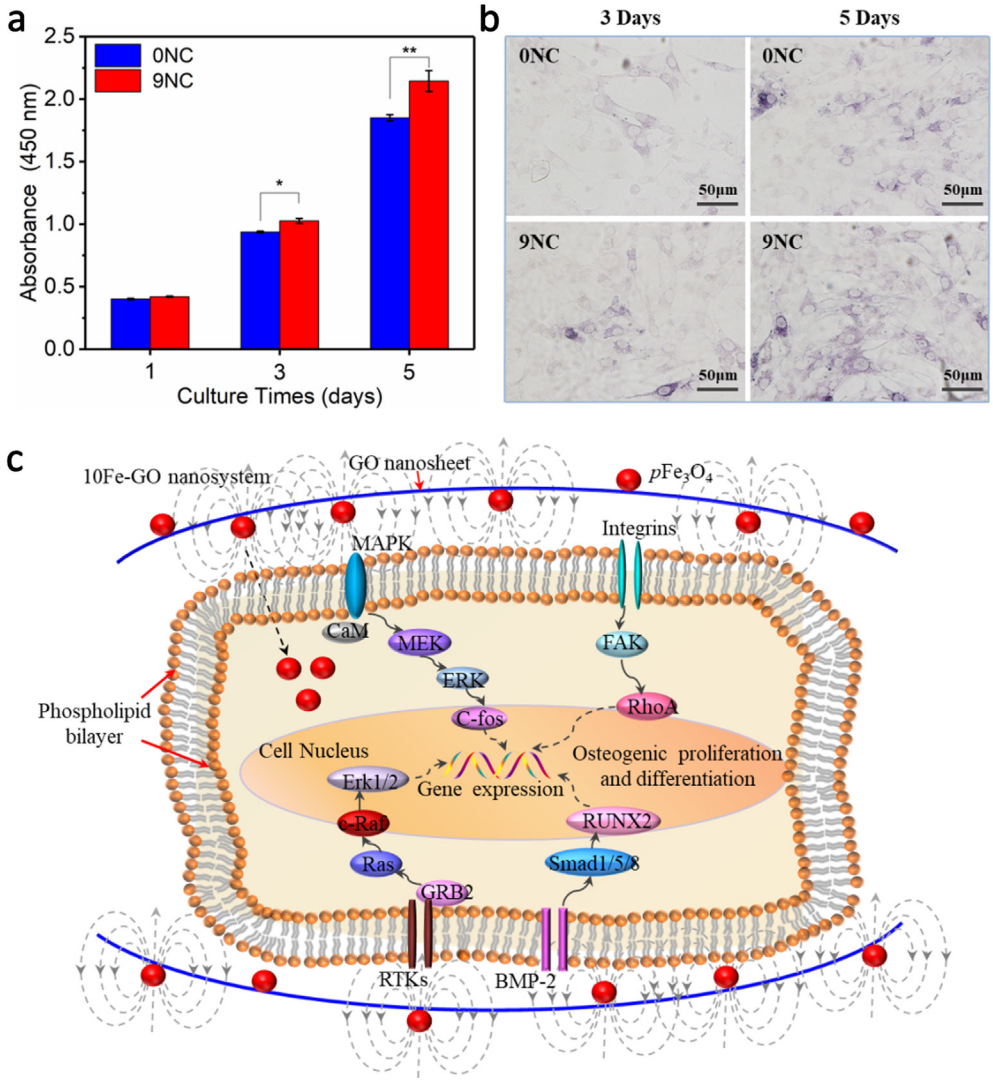

Fig. 9. (a) CCK-8 and (b) ALP activity analysis of MG63 cells after cultured on 0NC and 9NC scaffolds. (c) A schematic for a possible synergistic stimulation mechanism of 10Fe-GO nanosystem for osteogenic proliferation and differentiation, which combined the capturing effects of GO nanosheets and magnetic stimulation effects of pFe$_3$O$_4$ nanoparticles.

and capturing effects of GO nanosheets increased the local concentration of pFe$_3$O$_4$ nanoparticles around the cells due to that pFe$_3$O$_4$ were electrostatically self-assembled on GO, urging the cells to experience strong magnetic stimulation. The magnetic stimulation effect was mainly based on the nanoscale magnetic microenvironment provided by pFe$_3$O$_4$ nanoparticles, promoting cell adhesion and migration [56,57]. Subsequently, the magnetic microenvironment activated various signal pathways of cells, such as mitogen-activated protein kinase (MAPK), integrin, bone morphogenetic protein-2 (BMP-2) and receptor tyrosine kinases (RTKs) signal pathways [58–60], modulating the downstream genes of these pathways to enhance osteogenic proliferation and differentiation. As the cells grew into porous scaffold, the high retention and slow release of 10Fe-GO nanosystem provided longer and more sustained stimulation for cell growth and differentiation.

Conclusions

In this study, Fe$_3$O$_4$ was immersed in nitric acid to impart it positive charge via adsorbing hydrogen ions (H^+). Then, the positively charged Fe$_3$O$_4$ was assembled on negatively charged GO nanosheets to construct a co-dispersed nanosystem. The nanosystem was incorporated into PLLA scaffolds fabricated by SLS. The nanosystem synergistically enhanced the mechanical properties of scaffolds. The tensile strength of 9NC scaffolds was increased by 67.1% as well as the compressive strength and modulus were increased by 132% and 75.7%, respectively, with incorporating 9 wt% 10Fe-GO nanosystem. Moreover, the nanosystem synergistically enhanced the cell activity, proliferation and differentiation grown on the scaffolds, owing to the integration of the capturing effect of GO and the magnetic simulation effect of pFe$_3$O$_4$. Taken together, the scaffold may be expected to have potential applications in bone regeneration.

Compliance with ethics requirements

This article does not contain any studies with human or animal subjects.

Declaration of Competing Interest

The authors declare that they have no known competing financial interests or personal relationships that could have appeared to influence the work reported in this paper.

Acknowledgments

This study was supported by the following funds: (1) The Natural Science Foundation of China (51935014, 51905553, 81871494, 81871498, 51705540); (2) Hunan Provincial Natural Science Foundation of China (2019JJ50774, 2018JJ3671, 2019JJ50588); (3) JiangXi Provincial Natural Science Foundation of China (20192ACB20005); (4) Guangdong Province Higher Vocational Colleges & Schools Pearl River Scholar Funded Scheme (2018); (5) The Open Sharing Fund for the Large-scale Instruments and Equipments of Central South University; (6) The Project of Hunan Provincial Science and Technology Plan (2017RS3008).

References

[1] Feng P, Kong Y, Yu L, Li Y, Gao C, Peng S, et al. Molybdenum disulfide nanosheets embedded with nanodiamond particles: co-dispersion nanostructures as reinforcements for polymer scaffolds. Appl Mater Today 2019;17:216–26.
[2] Qian Y, Zhou X, Sun H, Yang J, Chen Y, Li C, et al. Biomimetic domain-active electrospun scaffolds facilitating bone regeneration synergistically with antibacterial efficacy for bone defects. ACS Appl Mater Interfaces 2018;10:3248–59.
[3] Shuai C, Yuan X, Yang W, Peng S, He C, Feng P, et al. Cellulose nanocrystals as biobased nucleation agents in poly-l-lactide scaffold: Crystallization behavior and mechanical properties. Polym Test 2020;85:106458.
[4] Yang W, Zhong Y, Feng P, Gao C, Peng S, Zhao Z, et al. Disperse magnetic sources constructed with functionalized Fe3O4 nanoparticles in poly-l-lactic acid scaffolds. Polym Test 2019;76:33–42.
[5] Awada H, Al Samad A, Laurencin D, Gilbert R, Dumail X, El Jundi A, et al. Controlled Anchoring of Iron Oxide Nanoparticles on Polymeric Nanofibers: Easy Access to Core@ Shell Organic-Inorganic Nanocomposites for Magneto-Scaffolds. ACS Appl Mater Interfaces 2019;11:9519–29.
[6] Cai Q, Shi Y, Shan D, Jia W, Duan S, Deng X, et al. Osteogenic differentiation of MC3T3-E1 cells on poly (l-lactide)/Fe3O4 nanofibers with static magnetic field exposure. Mater Sci Eng, C 2015;55:166–73.
[7] Yun H-M, Ahn S-J, Park K-R, Kim M-J, Kim J-J, Jin G-Z, et al. Magnetic nanocomposite scaffolds combined with static magnetic field in the stimulation of osteoblastic differentiation and bone formation. Biomaterials 2016;85:88–98.
[8] Shuai C, Feng P, Wu P, Liu Y, Liu X, Lai D, et al. A combined nanostructure constructed by graphene and boron nitride nanotubes reinforces ceramic scaffolds. Chem Eng J 2017;313:487–97.
[9] Shuai C, Zeng Z, Yang Y, Qi F, Peng S, Yang W, et al. Graphene oxide assists polyvinylidene fluoride scaffold to reconstruct electrical microenvironment of bone tissue. Mater Des 2020;190:108564.
[10] Song J, Gao H, Zhu G, Cao X, Shi X, Wang Y. The preparation and characterization of polycaprolactone/graphene oxide biocomposite nanofiber scaffolds and their application for directing cell behaviors. Carbon 2015;95:1039–50.
[11] Sang G, Dong J, He X, Jiang J, Li J, Xu P, et al. Electromagnetic interference shielding performance of polyurethane composites: A comparative study of GNs-IL/Fe_3O_4 and MWCNTs-IL/Fe_3O_4 hybrid fillers. Compos B Eng 2019;164:467–75.
[12] Shuai C, Guo W, Wu P, Yang W, Hu S, Xia Y, et al. A graphene oxide-Ag co-dispersing nanosystem: dual synergistic effects on antibacterial activities and mechanical properties of polymer scaffolds. Chem Eng J 2018;347:322–33.
[13] Nuona A, Li X, Zhu X, Xiao Y, Che J. Starch/polylactide sustainable composites: Interface tailoring with graphene oxide. Compos A Appl Sci Manuf 2015;69:247–54.
[14] Zou X, Zhang L, Wang Z, Luo Y. Mechanisms of the antimicrobial activities of graphene materials. J Am Chem Soc 2016;138:2064–77.
[15] Papageorgiou GZ, Terzopoulou Z, Bikiaris D, Triantafyllidis KS, Diamanti E, Gournis D, et al. Evaluation of the formed interface in biodegradable poly (L-lactic acid)/graphene oxide nanocomposites and the effect of nanofillers on mechanical and thermal properties. Thermochim Acta 2014;597:48–57.
[16] Gu S, Zhu A. Graphene nanosheets loaded Fe_3O_4 nanoparticles as a promising anode material for lithium ion batteries. J Alloy Compd 2020;813:152160.
[17] Han Q, Wang Z, Xia J, Chen S, Zhang X, Ding M. Facile and tunable fabrication of Fe_3O_4/graphene oxide nanocomposites and their application in the magnetic solid-phase extraction of polycyclic aromatic hydrocarbons from environmental water samples. Talanta 2012;101:388–95.
[18] Kang Y, Wang C, Qiao Y, Gu J, Zhang H, Peijs T, et al. Tissue-engineered trachea consisting of electrospun patterned sc-PLA/GO-g-IL fibrous membranes with antibacterial property and 3D-printed skeletons with elasticity. Biomacromolecules 2019;20:1765–76.
[19] Fu M, Jiao Q, Zhao Y, Li H. Vapor diffusion synthesis of $CoFe_2O_4$ hollow sphere/graphene composites as absorbing materials. J Mater Chem A 2014;2:735–44.
[20] Li X, Zhu H, Feng J, Zhang J, Deng X, Zhou B, et al. One-pot polylol synthesis of graphene decorated with size-and density-tunable Fe3O4 nanoparticles for porcine pancreatic lipase immobilization. Carbon 2013;60:488–97.
[21] Patil GP, Raut SS, Sankapal BR, Chavan PG. Anchoring of gold nanoparticles into aligned TiO2 nanotube: Improved supercapacitive performance. Nano-Struct Nano-Objects 2019;20:100381.
[22] Mohanty F, Swain SK. Nano silver embedded starch hybrid graphene oxide sandwiched poly (ethylmethacrylate) for packaging application. Nano-Struct Nano-Objects 2019;18:100300.
[23] Konni M, Dadhich AS, Mukkamala SB. Evaluation of surface changes at the interface between TiO2 nanoparticles and COOH-MWCNTs on hydrogen adsorption capability. Nano-Struct Nano-Objects 2019;18:100304.
[24] Zarnegar Z, Safari J, Zahraei Z. Design, synthesis and antimicrobial evaluation of silver decorated magnetic polymeric nanocomposites. Nano-Struct Nano-Objects 2019;19:100368.
[25] Nair AK, Bhavitha K, Perumbilavil S, Sankar P, Rouxel D, Kala M, et al. Multifunctional nitrogen sulfur co-doped reduced graphene oxide–Ag nano hybrids (sphere, cube and wire) for nonlinear optical and SERS applications. Carbon 2018;132:380–93.
[26] Deshmukh SP, Kale DP, Kar S, Shirsath SR, Bhanvase BA, Saharan VK, et al. Ultrasound assisted preparation of rGO/TiO_2 nanocomposite for effective photocatalytic degradation of methylene blue under sunlight. Nano-Struct Nano-Objects 2020;21:100407.
[27] Sharma M, Ramakrishnan S, Remanan S, Madras G, Bose S. Nano tin ferrous oxide decorated graphene oxide sheets for efficient arsenic (III) removal. Nano-Struct Nano-Objects 2018;13:82–92.
[28] Zhang Z-Z, Jiang D, Ding J-X, Wang S-J, Zhang L, Zhang J-Y, et al. Role of scaffold mean pore size in meniscus regeneration. Acta Biomater 2016;43:314–26.
[29] Lee SJ, Lee IW, Lee YM, Lee HB, Khang G. Macroporous biodegradable natural/synthetic hybrid scaffolds as small intestine submucosa impregnated poly (D, L-lactide-co-glycolide) for tissue-engineered bone. J Biomater Sci Polym Ed 2004;15:1003–17.
[30] Cojocaru FD, Balan V, Popa MI, Lobiuc A, Antoniac A, Antoniac IV, et al. Biopolymers-Calcium phosphates composites with inclusions of magnetic nanoparticles for bone tissue engineering. Int J Biol Macromol 2019;125:612–20.
[31] Yavari SA, van der Stok J, Chai YC, Wauthle R, Birgani ZT, Habibovic P, et al. Bone regeneration performance of surface-treated porous titanium. Biomaterials 2014;35:6172–81.
[32] Shuai C, Yang W, He C, Peng S, Gao C, Yang Y, et al. A magnetic micro-environment in scaffolds for stimulating bone regeneration. Mater Des 2019;185:108275.
[33] Shuai C, Cheng Y, Yang W, Feng P, Yang Y, He C, et al. Magnetically actuated bone scaffold: Microstructure, cell response and osteogenesis. Compos B Eng 2020;192:107986.
[34] Jose JP, Thomas S. XLPE based Al_2O_3–clay binary and ternary hybrid nanocomposites: self-assembly of nanoscale hybrid fillers, polymer chain confinement and transport characteristics. PCCP 2014;16:20190–201.
[35] Jose JP, Thomas S. Alumina–clay nanoscale hybrid filler assembling in cross-linked polyethylene based nanocomposites: mechanics and thermal properties. PCCP 2014;16:14730–40.
[36] Feng P, Jia J, Peng S, Yang W, Bin S, Shuai C. Graphene oxide-driven interfacial coupling in laser 3D printed PEEK/PVA scaffolds for bone regeneration. Virt Phys Prototyp 2020;15:1–16.
[37] Yang Y, Lu C, Peng S, Shen L, Wang D, Qi F, et al. Laser additive manufacturing of Mg-based composite with improved degradation behaviour. Virt Phys Prototyp 2020;15:1–16.
[38] Chen L, Chai S, Liu K, Ning N, Gao J, Liu Q, et al. Enhanced epoxy/silica composites mechanical properties by introducing graphene oxide to the interface. ACS Appl Mater Interfaces 2012;4:4398–404.
[39] Deeraj B, Harikrishnan R, Jayan JS, Saritha A, Joseph K. Enhanced visco-elastic and rheological behavior of epoxy composites reinforced with polyimide nanofiber. Nano-Struct Nano-Objects 2020;21:100421.
[40] Kundan K, Katti P, Kumar S, Bose S. Assessing the interfacial properties in carbon fiber/epoxy nanocomposites: from 'interlayers' to 'interconnects'. Nano-Struct Nano-Objects 2017;12:194–209.
[41] Shuai C, Wang B, Bin S, Peng S, Gao C. Interfacial strengthening by reduced graphene oxide coated with MgO in biodegradable Mg composites. Mater Des 2020;191:108612.
[42] Wang G, He C, Yang W, Qi F, Qian G, Peng S, et al. Surface-Modified Graphene Oxide with Compatible Interface Enhances Poly-L-Lactic Acid Bone Scaffold. J Nanomater 2020;2020:5634096.
[43] Jose JP, Chazeau L, Cavaillé J-Y, Varughese K, Thomas S. Nucleation and nonisothermal crystallization kinetics in cross-linked polyethylene/zinc oxide nanocomposites. RSC Adv 2014;4:31643–51.
[44] Wan S, Hu H, Peng J, Li Y, Fan Y, Jiang L, et al. Nacre-inspired integrated strong and tough reduced graphene oxide–poly (acrylic acid) nanocomposites. Nanoscale 2016;8:5649–56.
[45] Shuai C, Li Y, Yang W, Yu L, Yang Y, Peng S, et al. Graphene Oxide Induces Ester Bonds Hydrolysis of Poly-l-lactic Acid Scaffold to Accelerate Degradation. Int J Bioprint 2020;6:91–104.
[46] Feng P, Wu P, Gao C, Yang Y, Guo W, Yang W, et al. A multimaterial scaffold with tunable properties: toward bone tissue repair. Adv Sci 2018;5:1700817.
[47] Gao C, Yao M, Li S, Feng P, Peng S, Shuai C. Highly biodegradable and bioactive Fe-Pd-bredigite biocomposites prepared by selective laser melting. J Adv Res 2019;20:91–104.

[48] Sánchez-González S, Diban N, Urtiaga A. Hydrolytic degradation and mechanical stability of poly (ε-Caprolactone)/reduced graphene oxide membranes as scaffolds for in vitro neural tissue regeneration. Membranes 2018;8:12.
[49] Du X-C, Xu X-L, Liu X-H, Yang J-H, Wang Y, Gao X-L. Graphene oxide induced crystallization and hydrolytic degradation of poly (butylene succinate). Polym Degrad Stab 2016;123:94–104.
[50] Duan J, Xie Y-N, Yang J-H, Huang T, Zhang N, Wang Y, et al. Graphene oxide induced hydrolytic degradation behavior changes of poly (L-lactide) in different mediums. Polym Test 2016;56:220–8.
[51] Chen H-M, Feng C-X, Zhang W-B, Yang J-H, Huang T, Zhang N, et al. Hydrolytic degradation behavior of poly (l-lactide)/carbon nanotubes nanocomposites. Polym Degrad Stab 2013;98:198–208.
[52] Yang Y, He C, Dianyu E, Yang W, Qi F, Xie D, et al. Mg bone implant: Features, developments and perspectives. Mater Des 2020;185:108259.
[53] He S, Yang S, Zhang Y, Li X, Gao D, Zhong Y, et al. LncRNA ODIR1 inhibits osteogenic differentiation of hUC-MSCs through the FBXO25/H2BK120ub/H3K4me3/OSX axis. Cell Death Dis 2019;10:1–16.
[54] Cao L, Liu W, Zhong Y, Zhang Y, Gao D, He T, et al. Linc02349 promotes osteogenesis of human umbilical cord-derived stem cells by acting as a competing endogenous RNA for miR-25-3p and miR-33b-5p. Cell Proliferat 2020. doi: https://doi.org/10.1111/cpr.12814.
[55] Yan F, Liu Z, Zhang T, Zhang Q, Chen Y, Xie Y, et al. A biphasic injectable bone cement with Fe_3O_4/GO nanocomposites for the minimally invasive treatment of tumor-induced bone destruction. ACS Biomater Sci Eng 2019.
[56] Shuai C, Yang W, Peng S, Gao C, Guo W, Lai Y, et al. Physical stimulations and their osteogenesis-inducing mechanisms. Int. J. Bioprint 2018;4:138–58.
[57] Hu K, Zhou N, Li Y, Ma S, Guo Z, Cao M, et al. Sliced magnetic polyacrylamide hydrogel with cell-adhesive microarray interface: a novel multicellular spheroid culturing platform. ACS Appl Mater Interfaces 2016;8:15113–9.
[58] Zhu Y, Yang Q, Yang M, Zhan X, Lan F, He J, et al. Protein corona of magnetic hydroxyapatite scaffold improves cell proliferation via activation of mitogen-activated protein kinase signaling pathway. ACS Nano 2017;11:3690–704.
[59] Tang B, Zhuang J, Wang L, Zhang B, Lin S, Jia F, et al. Harnessing cell dynamic responses on magnetoelectric nanocomposite films to promote osteogenic differentiation. ACS Appl Mater Interfaces 2018;10:7841–51.
[60] Wang Q, Chen B, Cao M, Sun J, Wu H, Zhao P, et al. Response of MAPK pathway to iron oxide nanoparticles in vitro treatment promotes osteogenic differentiation of hBMSCs. Biomaterials 2016;86:11–20.